

Solitary waves criss-cross the quantum classical boundary

A. SREEDHARAN¹, S KURIYATTIL¹, S. CHOUDHURY^{1,2}, R. MUKHERJEE^{1,3}, A. STRELTSOV^{4,5} and S. WÜSTER¹

¹ Department of Physics, Indian Institute of Science Education and Research (IISER), Bhopal, Madhya Pradesh 462066, India

² New Zealand Institute for Advanced Study and Centre for Theoretical Chemistry and Physics, Massey University, Auckland 0632, New Zealand

³ Department of Physics, Imperial College, SW7 2AZ, London, UK

⁴ Theoretische Chemie, Physikalisch-Chemisches Institut, Universität Heidelberg, Im Neuenheimer Feld 229, D-69120 Heidelberg, Germany

⁵ SAP Deep Learning Center of Excellence and Machine Learning Research SAP SE, Dietmar-Hopp-Allee 16, 69190 Walldorf, Germany

Abstract – It is an open fundamental question how the classical appearance of our environment arises from the underlying quantum many-body theory. We propose that the quantum-classical boundary is probed in collisions of bright solitary waves in Bose-Einstein condensates, where thousands of atoms form a large compound object at ultra cold temperatures. For the experimentally most relevant Q1D regime, where integrability is broken through effective three-body interactions, we find that solitary waves appear to criss-cross the quantum classical boundary in beyond mean-field simulations using the truncated Wigner method. In a first crossing, an initial state with two solitons possessing well defined relative phase loses this phase coherence, appearing more classical. However we show that this apparent decoherence then can enable the formation of superpositions of different atom numbers in subsequent collisions of solitons. The necessity for the solitons to first decohere is explained based on the underlying phase-space of the quintic mean field equation. Superpositions of different atom numbers later evolve into spatially entangled solitons, creating highly non-classical states. Solitary waves thus appear to be crossing the quantum classical boundary a second time, in reverse.

Introduction. – Why most of the world around us follows the classical laws of physics, while being built from quantum mechanical microscopic constituents, is a paramount puzzle of modern physics [1,2]. As experiments are pushing towards superposition states with more and more constituents [3–12], all points to a central role of decoherence and system-environment entanglement in the transition from quantum to classical appearance [1,13,14].

These both inherently rely on the ease with which entanglement proliferates in quantum many body systems.

In ultra-cold gaseous Bose-Einstein condensates (BEC), thousands of atoms can form a compound object, a bright soliton [15], due to their weakly attractive contact interactions. These solitons are localized solutions of the Gross-Pitaevskii equation (GPE) that governs the mean field of the condensate [16–18]. They are protected from dispersion by the non-linearity of atomic interactions, and regularly created since 2002 [18–32], motivated by fundamental studies and applications in atom interferometry

[31,33,34].

Strictly, these bright solitons exists only in one dimension (1D), while all above experiments are in the quasi-1D (Q1D) regime, where transverse dynamics is important for atomic scattering, but not so much for describing bulk variables such as condensate density and phase. A crucial difference between the strictly 1D model and the Q1D one is that the integrability of the former Lieb-Liniger-MacGuire (LL) [35] is broken in Q1D through effective three-body interactions arising when atoms make virtual transitions to transverse modes [36–38].

Here, we show that some properties of solitons and soliton collisions can remain largely unaffected by integrability breaking, while other properties are dramatically altered. For typical experimental parameters [24], soliton shape [40] and fragmentation time-scales [41] are among the former, and different aspects of collision dynamics among the latter. A major qualitative change of dynamics in Q1D arises through new collision channels, in which

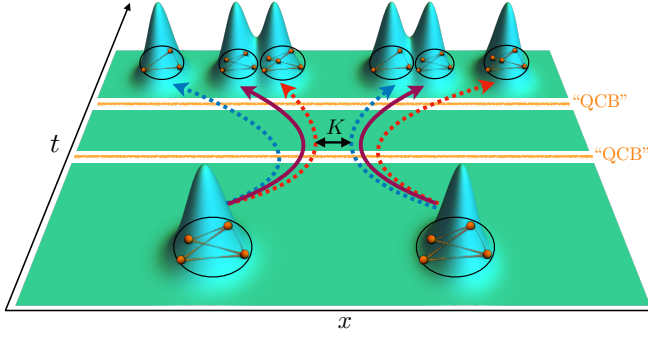


Fig. 1: Solitons criss-crossing the quantum-classical boundary (QCB, orange horizontal lines). Initially, two separated solitons fragment when losing phase coherence due to phase diffusion, which makes them appear more classical since collisions no longer depend on the initial relative phase [39]. However *only after* this initially dephasing, will the subsequent collision give rise to a state entangling atom number, momentum and position of both solitons (matching colored arrows) when atom transfer K due to integrability breaking in three dimensions is taken into account. Solitons thus appear to return to a highly non-classical state.

atomic population can transfer between the colliding solitons. Such transfer is prohibited in the strictly 1D Lieb-Liniger model, since an initial set of single particle momenta cannot be changed by collisions [42, 43]. Extending [39], our results explicitly take into account the integrability breaking interactions due to finite transverse size of the Bose gas, and employ the truncated Wigner approximation (TWA) [44–47] to represent the post-collision state sketched in Fig. 1.

As we shall show, in the emergent picture of a colliding pair of solitons these first loose mutual phase coherence, crossing the boundary from quantum mechanical behavior to a more classical one, only to then much more strongly entangle through number changing collisions. We thus propose that bright condensate solitons represent a versatile probe to explore the behavior of matter at the quantum classical boundary as they exhibit both, tuneable decoherence and tuneable generation of mesoscopic entanglement. Further their quantum dynamics shows the intriguing feature that solitons appear to cross the quantum-classical boundary (QCB), see Fig. 1, in two directions: Decohering initially and only subsequently seeing a generic proliferation of entanglement during collision, see Fig. 1. Unlike other probes of this boundary, we can continuously change the constituent atom number of a soliton N_{sol} , atomic interactions and thus internal soliton structure as well as decoherence. The latter can arise from coupling to an environment, which for cold atomic can be the same type of atoms, hotter and outside of the condensate.

Soliton collisions – Collisions of inert classical objects are typically fully governed by initial positions and momenta of collision partners. Quantum mechanically,

collisions might additionally depend on the quantum phases in the many-body wave function. The latter also play a central role in condensate soliton collisions, which are controlled by the relative phase φ and distance d between the colliding solitons in mean field theory. We write a twin soliton mean-field wave function as

$$\phi(x) = l(x)e^{ikx} + e^{i\varphi}r(x)e^{-ikx}, \quad (1)$$

with left and right soliton shapes $l(x) = \mathcal{N} \operatorname{sech}[(x + d/2)/\xi]$, $r(x) = \mathcal{N} \operatorname{sech}[(x - d/2)/\xi]$, where \mathcal{N} normalises each soliton to contain $N_{\text{sol}} = \int dx |l(x)|^2 = \int dx |r(x)|^2$ constituent atoms. The soliton widths are set by the healing length scale ξ , while solitons are a distance d apart with relative phase φ , k is the wave number associated with symmetric bulk soliton motion.

In 1D mean field theory, solitons evolve by the GPE,

$$i\hbar \frac{\partial}{\partial t} \phi(x, t) = \left[-\frac{\hbar^2}{2m} \frac{\partial^2}{\partial x^2} + \tilde{g}_{1D} |\phi(x, t)|^2 \right] \phi(x, t), \quad (2)$$

with 1D interaction strength $\tilde{g}_{1D} = 2a_s(\hbar\omega_{\perp}) = U_0/(2\pi\sigma_{\perp}^2) < 0$ derived from the 3D interaction strength $U_0 = \frac{4\pi\hbar^2 a_s}{m}$ and a transverse width $\sigma_{\perp} = \sqrt{\hbar/(m\omega_{\perp})}$. Here a_s is the scattering length, ω_{\perp} the transverse trapping frequency and m the atomic mass. For a simplified description, the Ansatz (1) can be inserted into (2) to derive effective equations of motion for $d(t)$ and $\varphi(t)$, predicting attractive collisions for $\varphi = 0$ and repulsive collisions for $\varphi = \pi$ [48, 49].

Beyond mean-field in the quasi-1D regime –

Here we go beyond Eq. (2), taking into account the effective modification of interactions by transverse modes in an elongated Q1D trap, and incorporating quantum correlations beyond mean field theory. It has been shown in [36–38], that the former give rise to an effectively one dimensional Hamiltonian

$$\hat{H} = \int dx \left\{ \hat{\Psi}^{\dagger}(x) \left[-\frac{\hbar^2}{2m} \frac{\partial^2}{\partial x^2} \right] \hat{\Psi}(x) + \frac{\tilde{g}_{1D}}{2} \hat{\Psi}^{\dagger}(x) \hat{\Psi}^{\dagger}(x) \hat{\Psi}(x) \hat{\Psi}(x) - \frac{\tilde{g}_2}{3} \hat{\Psi}^{\dagger}(x) \hat{\Psi}^{\dagger}(x) \hat{\Psi}^{\dagger}(x) \hat{\Psi}(x) \hat{\Psi}(x) \hat{\Psi}(x) \right\}. \quad (3)$$

The field operator $\hat{\Psi}(x)$ annihilates an atom of mass m at the longitudinal position x . Effective three body interactions scale with $\tilde{g}_2 = U_{\perp}/(3\pi^2\sigma_{\perp}^4) > 0$ from $U_{\perp} = 72 \ln(4/3) \frac{\hbar^3 a_s^2 \pi^2}{m^2 \omega_{\perp}^4}$ [38].

Using the usual techniques [44], we find the truncated Wigner equation of motion for the stochastic wavefunction $\phi_W(x, t)$ in Eq. (4) in a dimensionless form, by rescaling the wavefunction as $\phi_W \rightarrow \phi_W \sqrt{L}$, space as $x \rightarrow x/L$ and

time as $t \rightarrow t/T$ where $L = \sigma_\perp$ and $T = \omega_\perp^{-1}$:

$$i \frac{\partial}{\partial t} \phi_W = \left[-\frac{1}{2} \frac{\partial^2}{\partial x^2} + g_{1D} (|\phi_W|^2 - \delta_c) - q_2 (|\phi_W|^4 - 2|\phi_W|^2 \delta_c + \delta_c^2) \right] \phi_W. \quad (4)$$

The dimensionless interaction constants in (4) are $g_{1D} = 2a_s/\sigma_\perp$ and $q_2 = 24 \ln[\frac{4}{3}] a_s^2/\sigma_\perp^2$, and $\delta_c = \delta_c(x, x) \approx 1/dx$ is a restricted basis commutator [50] for grid-spacing dx .

Initially revisiting mean-field theory, we neglect δ_c and replace the stochastic wave-function $\phi_W(x)$ by the mean-field $\phi(x)$. Due to the quintic term, soliton shapes change from $l(x) \rightarrow L(x)$ and $r(x) \rightarrow R(x)$ in Eq. (1) such that [40]

$$R(x, t) = \sqrt{\frac{-4\mu\sqrt{3/(4q_2)}}{\sqrt{g^2 - 4\mu} \cosh[2\sqrt{-2\mu}(x - d(t))] + g}}, \quad (5)$$

using $g = -g_{1D}\sqrt{3/(4q_2)}$, and $L(x, t)$ similarly with $d(t) \rightarrow -d(t)$. The number of atoms in a soliton $N_{\text{sol}} = \sqrt{\frac{6}{q_2}} \arctan \left[\frac{2\sqrt{-\mu}}{g + \sqrt{g^2 - 4\mu}} \right]$ is controlled by the chemical potential $\mu < 0$. Soliton shapes are compared in Fig. 2 (a) for two different quintic interaction strengths q_2 . For experimentally relevant parameters of most interest to us, the difference between $L(x)$ and $l(x)$ is negligible. We hence shall also use $l(x)$ for some analytical results presented later, as indicated.

In the truncated Wigner approximation, we augment the initial state (1) with the above quintic soliton modes to a stochastic field $\phi_W(x)$, through the prescription

$$\phi_W(x, 0) = \phi_0(x) + \frac{1}{\sqrt{2}} \zeta(x), \quad (6)$$

where $\phi_0(x)$ is the initial mean field wavefunction and $\zeta(x)$ is a complex Gaussian distributed random function with correlations $\overline{\zeta(x)\zeta(x')} = 0$ and $\overline{\zeta^*(x)\zeta(x')} = \delta(x - x')$. The overline denotes the stochastic average. Quantum correlations are found through stochastic averages such as [47,51]

$$\langle \hat{\Psi}^\dagger(x) \hat{\Psi}(x') \rangle = \overline{\phi_W^*(x) \phi_W(x')} - \delta_c(x, x')/2, \quad (7)$$

where the field operator $\hat{\Psi}(x)$ annihilates an atom at position x .

For analytical insight, we will also consider a two-mode model (TMM) that arises from Eq. (3) by insertion of the ansatz $\hat{\Psi}(x, t) = \overline{L}[x, d(t)]\hat{a}(t) + \overline{R}[x, d(t)]\hat{b}(t)$ for the atomic quantum field, where \hat{a} destroys a boson in the left soliton, with mode function $\overline{L}(x, t) = L(x, t)/\sqrt{N_{\text{sol}}}$, and \hat{b} does the same for the right soliton. Each atom can thus be either in the left or the right soliton. The mode functions depend on time through the inter-soliton separation $d(t)$. Inserting the Ansatz into (3) and assuming large $d(t)$ so that modes $\overline{L}(x)$ and $\overline{R}(x)$ do not overlap, we reach a

simple time-dependent TMM Hamiltonian ($\hbar = m = 1$)

$$\hat{H} = \omega(\hat{a}^\dagger \hat{a} + \hat{b}^\dagger \hat{b}) + \frac{\chi}{2}(\hat{a}^\dagger \hat{a}^\dagger \hat{a} \hat{a} + \hat{b}^\dagger \hat{b}^\dagger \hat{b} \hat{b}) + \frac{\eta}{3}(\hat{a}^\dagger \hat{a}^\dagger \hat{a}^\dagger \hat{a} \hat{a} \hat{a} + \hat{b}^\dagger \hat{b}^\dagger \hat{b}^\dagger \hat{b} \hat{b} \hat{b}). \quad (8)$$

In (8), $\omega = \int dx |(\partial/\partial x) \overline{L}(x)|^2/2$ are single atom energies, and $\chi = g_{1D} \int dx |\overline{L}(x)|^4$, $\eta = -q_2 \int dx |\overline{L}(x)|^6$ capture the strength of interactions.

Three-body contribution to phase diffusion and mode shape – Whether the two soliton modes are phase coherent can be inferred from the eigenvalues $(2N_{\text{sol}})\bar{\lambda}_\pm$ of the one-body density matrix (OBDM) [52]

$$\varrho = \begin{bmatrix} \langle \hat{a}^\dagger \hat{a} \rangle & \langle \hat{b}^\dagger \hat{a} \rangle \\ \langle \hat{a}^\dagger \hat{b} \rangle & \langle \hat{b}^\dagger \hat{b} \rangle \end{bmatrix}. \quad (9)$$

If ϱ has one dominant eigenvalue $\bar{\lambda}_+ \approx 1$, all the atoms reside in the same *single* particle state (orbital), which can represent *two solitons* with complete phase coherence as in (1). Otherwise the system is fragmented with no phase-coherence between solitons [17, 41, 53], hence $\langle \hat{a}^\dagger \hat{b} \rangle = 0$. It was earlier shown that soliton trains fragment [41], which we could trace back to phase diffusion [54–56] in Ref. [39]. We now explore if this picture is modified through additional three-body interactions.

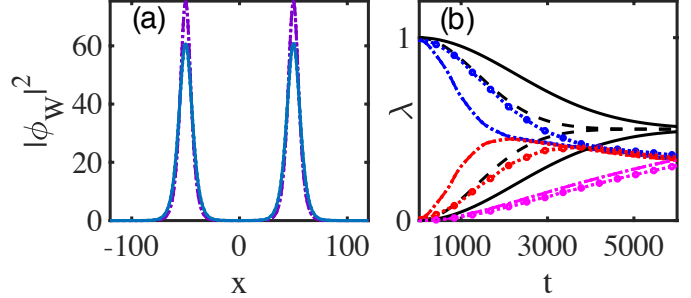


Fig. 2: Soliton shape and fragmentation of bright BEC solitons with quintic non-linearity, for $N_{\text{sol}} = 1000$, $g_{1D} = -2.3 \times 10^{-4}$ corresponding to a scattering length $a_s = -0.15$ nm and $\omega_\perp/(2\pi) = 800$ Hz (a) The mean density from TWA, $|\phi_W(x)|^2$ of a soliton pair, from Eq. (5), for two different quintic nonlinearities (light blue solid $q_2 = q_{2a} = 9.6 \times 10^{-8}$, violet dot-dashed $q_2 = q_{2b} = 7.68 \times 10^{-7}$). For $q_2 = 0$, the shape is indistinguishable from the light blue line. (b) Relative occupation $\bar{\lambda}_k$ of all system orbitals (eigenvalues of (9)) from TWA (colored lines) and TMM (black lines). We again compare q_{2a} (marked with \circ for TWA, black solid for TMM) and q_{2b} (without marker for TWA, black dashed for TMM). Blue marks the initially occupied orbital and red the second orbital participating in fragmentation. Magenta shows the sum of all other orbital populations in TWA. The sampling error for all TWA results is not visible on the scale of the plot.

For two far separated solitons, such that (8) is valid, we can evaluate the OBDM time-evolution, starting from both solitons in a coherent state with mean number N_{sol}

corresponding to a pure BEC. The solutions allow us to extract the relative occupation $\bar{\lambda}_{\pm}$ of the two system orbitals and hence degree of fragmentation as

$$\bar{\lambda}_{\pm} = \left(1 \pm e^{2N_{\text{sol}}[\cos(t/(2(N_{\text{sol}}-1)\eta+\chi))-1]} \right) / 2$$

$$\approx \left(1 \pm e^{-[t/t_{\text{frag}}]^2} \right) / 2, \quad (10)$$

where the expression after \approx is valid for short times. The system thus fragments on the timescale

$$t_{\text{frag}} = \left| \frac{1}{\sqrt{N_{\text{sol}}(2(N_{\text{sol}}-1)\eta+\chi)}} \right|. \quad (11)$$

For negligible quintic interactions, Eq. (11) reduces to the fragmentation time of the cubic model [39]. We see that in a general two-mode system, fragmentation can be accelerated or delayed, depending on the relative sign of cubic or quintic interactions. However for bright solitons $\chi, \eta < 0$, hence here the fragmentation process must be accelerated.

The TMM roughly agrees with the substantially more involved TWA regarding this time-scale and its dependence on η , as shown in Fig. 2 (b). For this comparison, we extract the OBDM $\rho(x, x') = \langle \hat{\Psi}^\dagger(x) \hat{\Psi}(x') \rangle$ from the TWA simulation and diagonalise it as a function of time, yielding eigenvalues $\lambda_k(t) = (2N_{\text{sol}})\bar{\lambda}_k(t)$. Initially, we have a pure BEC of two solitons since $\bar{\lambda}_+ = 1$. If two $\bar{\lambda}_k$, are of the order of unity, the system is fragmented. The figure shows, that as the strength of the quintic non-linearity increases, fragmentation occurs faster. The chosen examples show a considerable acceleration of fragmentation by stronger quintic interactions. However for parameters corresponding to recent experiments [24], we would have $(N_{\text{sol}}-1)\eta = -8.86 \times 10^{-7}$ compared to $\chi = -3.89 \times 10^{-6}$, thus the quintic contribution in Eq. (11) would have only a minor impact there. Our assumption of an elongated Q1D trap and the validity of the quintic correction model (8) require $N_{\text{sol}}\eta < \chi$, thus the fragmentation through phase diffusion can only appear mildly accelerated in general.

Atom transfer in soliton collisions – In contrast to the minor quantitative impact of three-body interactions on fragmentation times, they can cause qualitatively new features in quantum soliton collisions. To show this, we now study the interplay of fragmentation and collisions, using TWA. We separate the fragmentation and collision time-scales by forcing solitons to collide at a set time $t_{\text{coll}} = |d/(2v_{\text{ini}})|$, where d and v_{ini} are their initial distance and velocity. Since the noise added in Eq. (6) also causes an uncertainty of the soliton centre of mass (CM) and velocity [57,58], the collision time t_{coll} becomes uncertain. This is a distraction from our focus on the collision itself, hence we remove CM diffusion by post-processing the noisy initial state as discussed in Ref. [59]. Subsequent to this step, solitons collide at the target time t_{coll} for all realisations of the noise $\zeta(x)$. We also process time-evolving trajectories to remove those for which the

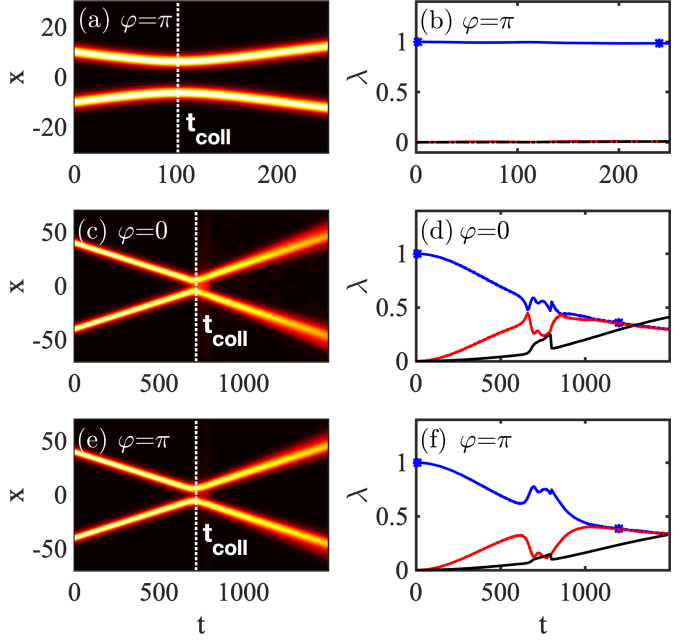


Fig. 3: Collision and coherence dynamics in controlled soliton collisions with three-body interactions, before fragmentation, at time $t_{\text{coll}} < t_{\text{frag}}$ (a-b) and after fragmentation, at time $t_{\text{coll}} > t_{\text{frag}}$ (c-f), with the same initial velocity $v_{\text{ini}} \approx 0.05$. We use $N_{\text{sol}} = 28000$, $g_{1D} = -2.53 \times 10^{-5}$ and $q_2 = 1.10 \times 10^{-9} \equiv \bar{q}_2$ unless otherwise indicated, corresponding to a scattering length $a_s = -0.030$ nm and $\omega_{\perp}/(2\pi) = 254$ Hz. The initial relative phases between solitons, φ , are indicated. (a,c,e) Total atomic density $n(x) = \langle \hat{\Psi}^\dagger(x) \hat{\Psi}(x) \rangle$ from TWA in (a) and squareroot of mean density to emphasize weak features in (c) and (e). (black, zero; bright, high). (b,d,f) The two largest orbital populations $\bar{\lambda}_k(t)$ from TWA (solid blue and red). The sum of the remaining populations is shown as a black line. Sampling errors are adjacent barely visible dotted lines.

number imbalance reaches $2a(t) = n_L(t) - n_R(t) > 10000$ from averages such as (7). This is to eliminate breathers and mergers as discussed in Ref. [59] and focus on collisions with a binary final state. In the expression above, $n_L(t) = \int_{-\infty}^0 dx n(x, t)$ is the total atom number on the left side of the spatial domain, n_R is the total number on the right.

The TWA now allows a more complete study of soliton motional and fragmentation dynamics than the methods employed Ref. [39], adding the effective three-body interactions $\sim q_2$ as shown in Fig. 3. The colour shading in Fig. 3 (a,c,e) indicates the mean atomic density $n(x) = \langle \hat{\Psi}^\dagger(x) \hat{\Psi}(x) \rangle$, obtained as in Eq. (7), averaging over $N_{\text{traj}} = 10000$ trajectories in (a) and $N_{\text{traj}} = 20000$ in (b) and (c). As discussed earlier, TWA also provides us the time evolution of the eigenvalues $\bar{\lambda}_k$ of the OBDM, shown in panels (b,d,f).

Prior to fragmentation, we find that solitons with $\varphi = \pi$ collide repulsively, as predicted by mean-field theory (2). The case $\varphi = 0$ is not shown, since it leads to a merger for these parameters [40]. After fragmentation, the col-

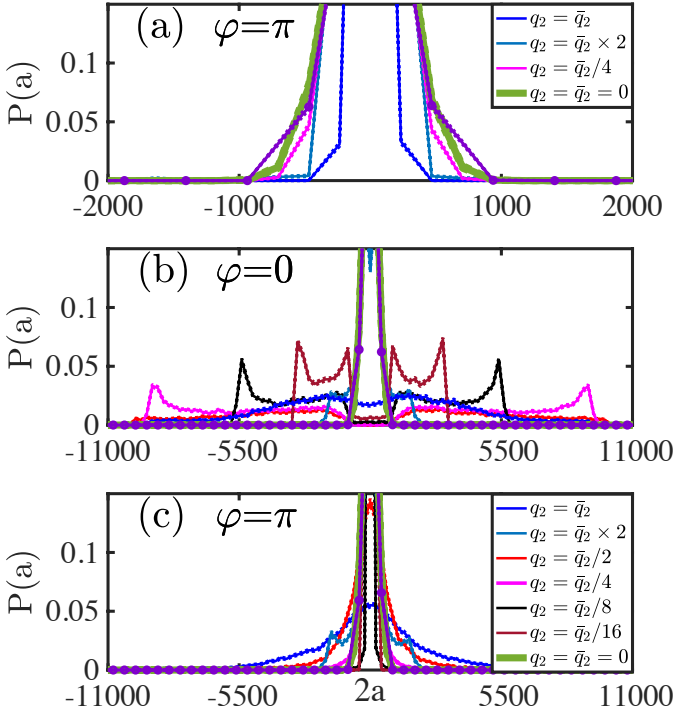


Fig. 4: The probability distributions for the atom number difference $2a = n_L - n_R$ from the TWA before collisions (violet lines with \bullet) and after collisions (blue), for parameters as in Fig. 3, corresponding to experiments in Ref. [24], which sets \bar{q}_2 . We then vary the strength of three-body interactions q_2 relative to the reference value \bar{q}_2 . Dotted lines close to solid lines indicate the sampling error. We compare collisions before fragmentation in (a) with those after fragmentation in (b,c). The green line in (a-c) is the post-collision distribution for vanishing quintic term, $\bar{q}_2 = 0$. The snapshots are at the times marked by (blue \star) in Fig. 3 before the collision (violet lines with \bullet) and after the collision (other lines).

lision appears repulsive for all φ . A new feature, exclusively enabled by three-body interactions, is the widened position uncertainty of solitons that collide after fragmentation. This can be seen upon close inspection of the total density in Fig. 3 (c,e), which appears more diffused after collisions. The cause are inelastic collisions, in which the outgoing soliton velocity is not equal to the incoming one.

To see this, we inspect the atom number distribution within solitons. Here, we encounter a major qualitative difference between collisions with and without three-body interactions, that constitutes our main result. Fig. 4 shows the distribution of the atom number difference $n_L - n_R$ before and after the collisions. For the case $q_2 = 0$, the distribution stays conserved, see green lines in panel (a). This feature is qualitatively changed by three-body interactions. While the distribution remains approximately conserved for the initial relative phase $\varphi = \pi$ and collisions prior to fragmentation, it is dramatically widened for all initial relative phases by collisions after fragmentation. We compare this effect in Fig. 4 for various values of q_2 , relative to the reference value \bar{q}_2 , (see Fig. 3) which rep-

resents the experimental parameters of Ref. [24], and find a non-monotonic dependence of the distribution width on q_2 .

Collisions with $q_2 \neq 0$ are dramatically different from those with $q_2 = 0$ because the quintic nonlinear term breaks the integrability of the TWA equations (4). While we had already reported atom transfer similar to Fig. 4 in Ref. [39], methods there broke integrability in an uncontrolled manner even for $q_2 = 0$. Here, the TWA captures both, integrability for $q_2 = 0$ and its breakdown through the same scattering terms that break it in soliton collision experiments of interest.

Since the completely one dimensional soliton collision with $q_2 = 0$ can be studied using the analytical solution of the LL model [35, 60] as in Refs. [42, 43], it is tempting to corroborate the unlocking of inter-soliton atom transfer by $q_2 \neq 0$ also in that framework. We found that approach quickly intractable when trying to handle localized solitons, but could show the non-vanishing of the matrix element of three-body interactions between a state with two delocalized solitons with atom numbers $(N_{\text{sol}}, N_{\text{sol}})$ and momenta $(p_0, -p_0)$ [42, 43] and one with numbers $(N_{\text{sol}} - k, N_{\text{sol}} + k)$ and momenta (p'_1, p'_2) such that the total momentum is conserved.

We now further go beyond the results of Ref. [39], to explain why atom transfer in Fig. 4 is only prominent after fragmentation and not before. To this end, we use a phase-space picture for the single stochastic trajectories arising from (4), discussed in the next section.

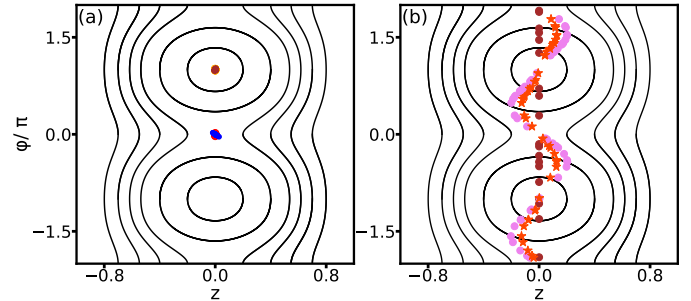


Fig. 5: (a,b) Phase-space portrait (black lines) for population imbalance z and inter-soliton phase difference φ , governing Eqs. (12a) and (12b) for parameters guided by Fig. 3 and Fig. 4. We took a fixed distance $d = 11$ corresponding to the closest approach in Fig. 3. Then $\chi = -2.9 \times 10^{-6}$, $\eta = -1.8 \times 10^{-11}$, $\bar{U} = -4.3 \times 10^{-8}$, $\bar{T} = -1.8 \times 10^{-7}$, $\bar{K} = 2.2 \times 10^{-14}$, $\tilde{K} = 7.5 \times 10^{-14}$, $\tilde{J} = 9.4 \times 10^{-13}$ and $K = -0.0049$ [61]. Superimposed, we show (a) Trajectories corresponding to collisions before fragmentation for initial relative phase close to $\varphi = 0$ (red \bullet at $t = 0$, blue \bullet at $t = 25$), and for initial relative phase close to $\varphi = \pi$ (orange \bullet at $t = 0$, brown \bullet at $t = 25$). (b) Trajectories corresponding to collisions after complete fragmentation with random initial relative phase (brown \bullet at $t = 0$, violet \bullet at $t = 25$, red \bullet at $t = 25$ with $q_2 \rightarrow 2\bar{q}_2$, with \bar{q}_2 defined in Fig. 3).

Fragmentation enhances atom transfer – To understand the different atom transfer probabilities before and after fragmentation, we move to the two-mode mean-field model for a soliton pair, writing $\phi(x, t) = \psi_L(t)\bar{l}(x, d_0) + \psi_R(t)\bar{r}(x, d_0)$ for a representative fixed d_0 , with time-dependent amplitudes $\psi_{L,R}(t) = \sqrt{N_{L,R}}e^{i\theta_{L,R}(t)}$, where $\bar{l}(x, t) = l(x, t)/\sqrt{N_{\text{sol}}}$, $N_{L,R}$ and $\theta_{L,R}$ are the number of atoms and phases of left and right soliton respectively. We insert this restricted ansatz into the mean field version of Eq. (4) and following [62], rewrite the result in terms of the fractional population imbalance $z = (N_L - N_R)/(2N_{\text{sol}})$ and inter-soliton phase difference $\varphi = \theta_R - \theta_L$, to reach equations of motion

$$\begin{aligned} \dot{z} = & \left\{ 2N_{\text{tot}}(\bar{U} + 2\tilde{K}N_{\text{tot}})(1 - z^2) \cos(\varphi) \right. \\ & - \sqrt{1 - z^2} \left[2K - 2N_{\text{tot}}\bar{T} - N_{\text{tot}}^2 \left[\tilde{J}(1 + z^2) \right. \right. \\ & \left. \left. + \bar{K}[2 + \cos(2\varphi)](1 - z^2) \right] \right] \right\} \sin(\varphi), \end{aligned} \quad (12a)$$

$$\begin{aligned} \dot{\varphi} = & \frac{z}{2\sqrt{1 - z^2}} \left\{ 2N_{\text{tot}}\sqrt{1 - z^2} \left(\chi - 2\bar{U} - N_{\text{tot}}(\eta + 3\tilde{K}) \right) \right. \\ & + \left[4K - 4N_{\text{tot}}\bar{T} + N_{\text{tot}}^2 \left[\tilde{J}(2 - 6z^2) - 9\bar{K}(1 - z^2) \right] \right] \\ & [\cos(\varphi)] - 2N_{\text{tot}} \left(2N_{\text{tot}}\tilde{K} + \bar{U} \right) \sqrt{1 - z^2} \cos(2\varphi) \\ & \left. - \bar{K}N_{\text{tot}}^2(1 - z^2) \cos(3\varphi) \right\}, \end{aligned} \quad (12b)$$

where $N_{\text{tot}} = 2N_{\text{sol}}$ and only η and χ , defined earlier, are independent of the distance d . In contrast, defining the integral $O(\alpha, \beta) = \int dx \bar{l}(x)^\alpha \bar{r}(x)^\beta$, we have $\bar{U} = g_{1D}O(2, 2)$, $\bar{T} = g_{1D}O(3, 1)$, $\tilde{K} = q_2O(4, 2)$, $K = q_2O(3, 3)$, $\tilde{J} = q_2O(5, 1)$, which all depend on d , as does $\bar{K} = \int dx (\partial/\partial x)\bar{l}(x)(\partial/\partial x)\bar{r}(x)/2$, χ and η has the same form as before with $\bar{L}(x) \rightarrow \bar{l}(x)$ and $\bar{R}(x) \rightarrow \bar{r}(x)$. Since Eq. (12) can be derived from an effective Hamiltonian as in Ref. [62], solutions for different initial conditions create a phase space portrait for the two dynamical variables z and φ , shown in Fig. 5 as thin black lines.

To understand our TWA results in Fig. 4, we view the stochastic realisations of (4) as noisy trajectories in this phase-space. When projecting onto the two-mode problem Eq. (12), the noise $\zeta(x)$ contained in $\phi_W(x, t = 0)$ effectively causes a randomisation of the initial population imbalance $z(0)$ and initial relative phase $\varphi(0)$. This can be modelled by a swarm of trajectories in the phase space of Fig. 5, for which the initial distributions of $z(0)$ and $\varphi(0)$ roughly correspond to those in Fig. 4. We extract a Gaussian fit for these two, $p(z) \sim e^{-z^2/(2\sigma_z^2)}$ and similarly for φ , and find $\sigma_z = \frac{247.48}{N_{\text{tot}}}$ and $\sigma_\varphi = 0.045\pi$ for the distributions prior to collision in Fig. 4.

We then use a corresponding ensemble of initial conditions as shown in Fig. 5(a), normally distributed around

$z(0) = 0, \phi(0) = 0$ (red swarm of points) and $z(0) = 0, \phi(0) = \pi$ (orange swarm of points), to understand how phase differences affect atom transfer prior to fragmentation. At a later time $t = 25$, roughly corresponding to the duration of the collision in Fig. 3, we find that the trajectories starting near $z(0) = 0$ and $\phi(0) = 0$ move only slightly away from the unstable fixed point (blue points), while those starting near $z(0) = 0$ and $\phi(0) = \pi$ remain close to the stable fixed point (brown points), as expected from the underlying phase space structure. Neither depart significantly from the line $z = 0$, which that the pre-fragmentation scenario in Fig. 4 (a) shows negligible atom transfer.

To understand atom transfer after fragmentation, we follow a similar approach. A fragmented state can be described as a weighted average of coherent states [53]. To represent a completely unknown relative phase, we thus start with a uniform random distribution of all relative phase differences $\phi \in [-\pi, \pi]$, retaining the same distribution of $z(0)$ used earlier (brown swarm of points). Here we find a large fraction of the trajectories moving significantly away from the line $z = 0$ by $t = 25$ (violet points), due to the structure of phase space. This explains the significant widening of the number distribution after fragmentation in Fig. 4 (b,c). We also capture the feature of Fig. 4, that increasing q_2 does not necessarily lead to a wider final distribution, see red points. This is due to cancellations among the TMM coefficients.

For the results in Fig. 5, the evolution times t roughly correspond to the duration τ of collisions in Fig. 3 and also the TMM parameters match that scenario. It is thus encouraging that the variances of distributions for z obtained almost quantitatively match those shown in Fig. 4. However one must bear in mind that the real soliton collision trajectory gives rise to a time-dependent $d(t)$ and thus time-dependent phase space structure, which will complicate the intuitive picture above. Coefficients in Eq. (12) can also change sign depending on d , which causes a swap of stable and unstable fixed points.

Criss-crossing the quantum classical boundary – After the significant widening of the atom number distribution during a collision of bright solitons that we demonstrated in Fig. 4 and explained through Fig. 5, an immediate consequence for the post-collision period $t > t_{\text{coll}}$ must now be the generation of entanglement. The model (3) conserves energy and momentum. If one soliton gains atoms at the expense of the other, momentum conservation requires it to move more slowly afterwards. One can then infer a post-collision velocity $v(n_s)$ for a soliton as a function of its constituent atom number n_s from energy and momentum conservation, such that the total post-collision many-body state has the schematic structure

$$\begin{aligned} |\Psi_{\text{pc}}\rangle = & \sum_{n_s} c_{n_s} |n_s, v(n_s)\rangle_L \\ & \otimes |2N_{\text{sol}} - n_s, v(2N_{\text{sol}} - n_s)\rangle_R, \end{aligned} \quad (13)$$

shown in Fig. 1 (c). The states $|n_s, v\rangle$ in Eq. (13) indicate a many-body state for n_s atoms forming a soliton, which moves with velocity v and c_{n_s} are complex coefficients, for which $p(n_s) = |c_{n_s}|^2$ is shown in Fig. 4. For a wide distribution $p(n_s)$ the atom number in the left soliton is entangled with the right one [63].

The schematic (13) constitutes the many-body generalisation of semi-classical results in Ref. [64], reminiscent of the collision induced two species Bell states proposed in [65] and entanglement generation involving dark [66] or dark-bright solitons [67]. It in fact goes beyond these in representing a hyper-entangled [68] soliton state, as we demonstrate in [59]. There we also discuss how the conversion of number entanglement into position and momentum entanglement leads to the widening of position distributions discussed in Fig. 3.

Conclusions and outlook – We have studied collisions of BEC bright solitary waves, explicitly including effective three-body interactions that break integrability in the Q1D setting [36–38]. While fragmentation due to phase-diffusion and soliton mode shapes are typically not significantly affected by these interactions for realistic parameters, we show that the collision dynamics changes qualitatively compared to the description neglecting these contributions. While the atom number within each soliton is conserved during a collision with only two-body interactions, we demonstrate a significant change of its distribution when three-body interactions are included, using the truncated Wigner approximation.

We also explained why fragmentation is a prior requirement for this atom transfer when starting from a repulsive relative phase $\varphi = \pi$ from the phase-space structure of the noisy mean field model. The two-soliton many-body state *first* has to loose coherence between the left and right soliton through phase-diffusion. In this step, solitons thus appear to traverse the quantum-classical boundary to appear more classical. Then, *only after* this initial crossing, will quantum many-body dynamics during the collision lead to the extremely entangled state (13). In that sense, the collision leads to a second traversal of the boundary back into the quantum domain. Of course quantifying classicality in the above is highly observable dependent, since the complete many-body state evolves unitarily. Our intention with the interpretation given, is to highlight that colliding bright solitons appear promising to gain a deeper understanding of the quantum-classical boundary, owing to their relatively simple underlying Hamiltonian (3), yet complex emergent collision behaviour. For the simulations in Fig. 3, Fig. 4 and Fig. 5, where we demonstrated these features, we have chosen experimentally realistic parameters guided by Ref. [24].

We gladly acknowledge the Max-Planck society for funding under the MPG-IISER partner group program.

SK thanks Abhijit Pendse for discussions regarding Lieb-Liniger Model. ASR acknowledges the Department of Science and Technology (DST), New Delhi, India, for the INSPIRE fellowship IF160381.

REFERENCES

- [1] SCHLOSSHAUER M., *Rev. Mod. Phys.*, **76** (2005) 1267.
- [2] SCHLOSSHAUER M. A., *Decoherence and the quantum-to-classical transition* (Springer) 2007.
- [3] FRIEDMAN J. R., PATEL V., CHEN W., TOLPYGO S. and LUKENS J. E., *Nature*, **406** (2000) 43.
- [4] GAO W.-B., LU C.-Y., YAO X.-C., XU P., GÜHNE O., GOEBEL A., CHEN Y.-A., PENG C.-Z., CHEN Z.-B. and PAN J.-W., *Nat. Phys.*, **6** (2010) 331.
- [5] LEIBFRIED D., KNILL E., SEIDELIN S., BRITTON J., BLAKESTAD R. B., CHIAVERINI J., HUME D. B., ITANO W. M., JOST J. D., LANGER C., OZERI R., REICHLE R. and WINELAND D. J., *Nature*, **438** (2005) 639.
- [6] TAKAHASHI H., WAKUI K., SUZUKI S., TAKEOKA M., HAYASAKA K., FURUSAWA A. and SASAKI M., *Phys. Rev. Lett.*, **101** (2008) 233605.
- [7] GERLICH S., EIBENBERGER S., TOMANDL M., NIMMRICHTER S., HORNBERGER K., FAGAN P. J., TÜXEN J., MAYOR M. and ARNDT M., *Nat. Commun.*, **2** (2011) 263.
- [8] LU C.-Y., ZHOU X.-Q., GÜHNE O., GAO W.-B., ZHANG J., YUAN Z.-S., GOEBEL A., YANG T. and PAN J.-W., *Nat. Phys.*, **3** (2007) 91.
- [9] MONROE C., MEEKHOF D. M., KING B. E. and WINELAND D. J., *Science*, **272** (1996) 1131.
- [10] ARNDT M., NAIRZ O., VOS-ANDREAE J., KELLER C., VAN DER ZOUW G. and ZEILINGER A., *Nature*, **401** (1999) 680.
- [11] ARNDT M. and HORNBERGER K., *Nat. Phys.*, **10** (2014) 271.
- [12] EIBENBERGER S., GERLICH S., ARNDT M., MAYOR M. and TÜXEN J., *Phys. Chem. Chem. Phys.*, **15** (2013) 14696.
- [13] HACKERMÜLLER L., HORNBERGER K., BREZGER B., ZEILINGER A. and ARNDT M., *Nature*, **427** (2004) 711.
- [14] HORNBERGER K., UTTENTHALER S., BREZGER B., HACKERMÜLLER L., ARNDT M. and ZEILINGER A., *Phys. Rev. Lett.*, **90** (2003) 160401.
- [15] The BEC solitons in question are solitary waves throughout this article.
- [16] KIVSHAR Y. S. and AGRAWAL G. P., *Optical Solitons: From Fibers to Photonic Crystals* (Academic, San Diego) 2003.
- [17] PETHICK C. J. and SMITH H., *Bose-Einstein condensation in dilute gases* (Cambridge University Press) 2002.
- [18] STRECKER K. E., PARTRIDGE G. B., TRUSCOTT A. G. and HULET R. G., *New J. Phys.*, **5** (2003) 73.
- [19] KHAYKOVICH L., SCHRECK F., FERRARI G., BOURDEL T., CUBIZOLLES J., CARR L. D., CASTIN Y. and SALOMON C., *Science*, **296** (2002) 1290.
- [20] STRECKER K. E., PARTRIDGE G. B., TRUSCOTT A. G. and HULET R. G., *Nature*, **417** (2002) 150.
- [21] EIERMANN B., ANKER T., ALBIEZ M., TAGLIEBER M., TREUTLEIN P., MARZLIN K.-P. and OBERTHALER M. K., *Phys. Rev. Lett.*, **92** (2004) 230401.

[22] CORNISH S. L., THOMPSON S. T. and WIEMAN C. E., *Phys. Rev. Lett.*, **96** (2006) 170401.

[23] NGUYEN J. H. V., LUO D. and HULET R. G., *Science*, **356** (2017) 422.

[24] NGUYEN J. H. V., DYKE P., LUO D., MALOMED B. A. and HULET R. G., *Nat. Phys.*, **10** (2014) 918.

[25] MARCHANT A. L., BILLAM T. P., YU M. M. H., RAKON-JAC A., HELM J. L., POLO J., WEISS C., GARDINER S. A. and CORNISH S. L., *Phys. Rev. A*, **93** (2016) 021604(R).

[26] MARCHANT A. L., BILLAM T. P., WILES T. P., YU M. M. H., GARDINER S. A. and CORNISH S. L., *Nat. Commun.*, **4** (2013) 1865.

[27] MEDLEY P., MINAR M. A., CIZEK N. C., BERRYRIESER D. and KASEVICH M. A., *Phys. Rev. Lett.*, **112** (2014) 060401.

[28] LEPOUTRE S., FOUCHE L., BOISSÉ A., BERTHET G., SALOMON G., ASPECT A. and BOURDEL T., *Phys. Rev. A*, **94** (2016) 053626.

[29] McDONALD G. D., KUHN C. C. N., HARDMAN K. S., BENNETTS S., EVERITT P. J., ALTIN P. A., DEBS J. E., CLOSE J. D. and ROBINS N. P., *Phys. Rev. Lett.*, **113** (2014) 013002.

[30] EVERITT P. J., SOORIYABANDARA M. A., GUASONI M., WIGLEY P. B., WEI C. H., McDONALD G. D., HARDMAN K. S., MANJU P., CLOSE J. D., KUHN C. C. N., SZIGETI S. S., KIVSHAR Y. S. and ROBINS N. P., *Phys. Rev. A*, **96** (2017) 041601(R).

[31] MEŽNARŠIČ T., ARH T., BRENCE J., PIŠLJAR J., GOSAR K., GOSAR I. C. V., ŽITKO R., ZUPANIČ E. and JEGLIČ P., *Phys. Rev. A*, **99** (2019) 033625.

[32] SANZ J., FRÖLIAN A., CHISHOLM C., CABRERA C. and TARRUELL L., *Phys. Rev. Lett.*, **128** (2022) 013201.

[33] TSAREV D. V., ARAKELIAN S. M., CHUANG Y.-L., LEE R.-K. and ALODJANTS A. P., *Opt. Express*, **26** (2018) 19583.

[34] TSAREV D. V., NGO T. V., LEE R.-K. and ALODJANTS A. P., *New J. Phys.*, **21** (2019) 083041.

[35] LIEB E. H. and LINIGER W., *Phys. Rev.*, **130** (1963) 1605.

[36] MURYSHEV A., SHLYAPNIKOV G. V., ERTMER W., SENGSTOCK K. and LEWENSTEIN M., *Phys. Rev. Lett.*, **89** (2002) 110401.

[37] SINHA S., CHERNY A. Y., KOVRIZHIN D. and BRAND J., *Phys. Rev. Lett.*, **96** (2006) 030406.

[38] MAZETS I. E., SCHUMM T. and SCHMIEDMAYER J., *Phys. Rev. Lett.*, **100** (2008) 210403.

[39] SREEDHARAN A., CHOUDHURY S., MUKHERJEE R., STRELTSOV A. and WÜSTER S., *Phys. Rev. A*, **101** (2020) 043604.

[40] KHAYKOVICH L. and MALOMED B. A., *Phys. Rev. A*, **74** (2006) 023607.

[41] STRELTSOV A. I., ALON O. E. and CEDERBAUM L. S., *Phys. Rev. Lett.*, **106** (2011) 240401.

[42] LAI Y. and HAUS H. A., *Phys. Rev. A*, **40** (1989) 844.

[43] LAI Y. and HAUS H. A., *Phys. Rev. A*, **40** (1989) 854.

[44] STEEL M. J., OLSEN M. K., PLIMAK L. I., DRUMMOND P. D., TAN S. M., COLLETT M. J., WALLS D. F. and GRAHAM R., *Phys. Rev. A*, **58** (1998) 4824.

[45] SINATRA A., LOBO C. and CASTIN Y., *Phys. Rev. Lett.*, **87** (2001) 210404.

[46] SINATRA A., LOBO C. and CASTIN Y., *J. Phys. B: At. Mol. Opt. Phys.*, **35** (2002) 3599.

[47] BLAKIE P., BRADLEY A., DAVIS M., BALLAGH R. and GARDINER C., *Adv. Phys.*, **57** (2008) 363.

[48] GORDON J. P., *Opt. Lett.*, **8** (1983) 596.

[49] AL-KHAWAJA U., STOOF H. T. C., HULET R. G., STRECKER K. E. and PARTRIDGE G. B., *Phys. Rev. Lett.*, **89** (2002) 200404.

[50] NORRIE A. A., BALLAGH R. J. and GARDINER C. W., *Phys. Rev. A*, **73** (2006) 043617.

[51] GARDINER C. W. and ZOLLER P., *Quantum Noise*, 3rd ed. (Springer-Verlag, Berlin Heidelberg,) 2004.

[52] PENROSE O. and ONSAGER L., *Phys. Rev. A*, **104** (1956) 576.

[53] MUELLER E. J., HO T. L., UEDA M. and BAYM G., *Phys. Rev. A*, **74** (2006) 033612.

[54] LEWENSTEIN M. and YOU L., *Phys. Rev. Lett.*, **77** (1996) 3489.

[55] MENOTTI C., ANGLIN J. R., CIRAC J. I. and ZOLLER P., *Phys. Rev. A*, **63** (2001) 023601.

[56] HAINE S. A., *New J. Phys.*, **20** (2018) 033009.

[57] COSME J. G., WEISS C. and BRAND J., *Phys. Rev. A*, **94** (2016) 043603.

[58] WEISS C., GARDINER S. A. and BREUER H.-P., *Phys. Rev. A*, **91** (2015) 063616.

[59] SREEDHARAN A., SRIDEVI K. and WÜSTER S., arXiv:2202.06120 (2022).

[60] MCGUIRE J. B., *J. Math. Phys.*, **5** (1964) 622.

[61] For those parameters, terms \tilde{K} and \bar{K} could have been neglected.

[62] SMERZI A., FANTONI S., GIOVANAZZI S. and SHENOY S. R., *Phys. Rev. Lett.*, **79** (1997) 4950–4953.

[63] NG K. L., OPANCHUK B., REID M. D. and DRUMMOND P. D., *Phys. Rev. Lett.*, **122** (2019) 203604.

[64] LEWENSTEIN M. and MALOMED B. A., *New J. Phys.*, **11** (2009) 113014.

[65] GERTJERENKEN B., BILLAM T. P., BLACKLEY C. L., LE SUEUR C. R., KHAYKOVICH L., CORNISH S. L. and WEISS C., *Phys. Rev. Lett.*, **111** (2013) 100406.

[66] MISHMASH R. V. and CARR L. D., *Phys. Rev. Lett.*, **103** (2009) 140403.

[67] KATSIMIGA G. C., KOUTENTAKIS G. M., MISTAKIDIS S. I., KEVREKIDIS P. G. and SCHMELCHER P., *New J. Phys.*, **19** (2017) 073004.

[68] KWIAT P. G., *J. Mod. Opt.*, **44** (1997) 2173.